Accounting for Vertical Subgrid-Scale Heterogeneity in Low-Level Cloud Fraction Parameterizations

Jean-Louis Dufresne, J. Jouhaud, J.-l. Dufresne, J.-b. Madeleine, F. Hourdin, Fleur Couvreux, N. Villefranque, A. Jam

AGU100 ADVANCING EARTH AND SPACE SCIENCE

Journal of Advances in Modeling Earth Systems

RESEARCH ARTICLE
10.1029/2018MS001379

Key Points:
- Most cloud schemes assume vertically homogeneous cloud fractions in GCM grid boxes
- This approximation may induce an underestimation of cloud cover and overestimation of reflectance
- We parameterize 3-D subgrid-scale heterogeneities for low-level clouds and reduce these biases

Correspondence to:
J. Jouhaud,
jean.jouhaud@gmail.com

Citation:
Jouhaud, J., Dufresne, J.-L., Madeleine, J.-B., Hourdin, F., Couvreux, F., Villefranque, N., & Jam, A. (2018). Accounting for vertical subgrid-scale heterogeneity in low-level cloud fraction parameterizations. *Journal of Advances in Modeling Earth Systems*, *10*, 2686–2705. https://doi.org/10.1029/2018MS001379

Received 18 MAY 2018
Accepted 21 SEP 2018
Accepted article online 2 OCT 2018
Published online 5 NOV 2018

Accounting for Vertical Subgrid-Scale Heterogeneity in Low-Level Cloud Fraction Parameterizations

J. Jouhaud[1], J.-L. Dufresne[1], J.-B. Madeleine[1], F. Hourdin[1], F. Couvreux[2], N. Villefranque[2], and A. Jam[1]

[1]Laboratoire de Météorologie Dynamique/IPSL, CNRS, Sorbonne Université, École Normale Supérieure, PSL Research University, École polytechnique, Paris, France, [2]CNRM, Université de Toulouse, Météo-France, CNRS, Toulouse, France

Abstract Many general circulation models (GCMs) assume some heterogeneity of water amounts in their grid boxes and use probability density functions to parameterize cloud fractions *CF* and amounts of condensed water q_c. Most GCM cloud schemes calculate the CF as the volume of the grid box that contains clouds (CF_{vol}), whereas radiative fluxes primarily depend on the CF by surface (CF_{surf}), that is, the surface of the grid box covered by clouds when looking from above. This discrepancy matters as previous findings suggest that *CF*surf is typically greater than CF_{vol} by about 30%. In this paper we modify the single column model version of the LMDz GCM cloud scheme by introducing the vertical subgrid-scale heterogeneity of water content. This allows to distinctly compute the two fractions, CF_{vol} and CF_{surf}, as well as the amount of condensed water q_c. This study is one of the first to take into account such vertical subgrid-scale heterogeneity in a GCM cloud scheme. Three large eddy simulation cases of cumuliform boundary layer clouds are used to test and calibrate two different parameterizations. These new developments increase cloud cover by about 10% for the oceanic cases RICO and Barbados Oceanographic Meteorological Experiment and by up to 50% for the continental case ARM. The change in condensed water reduces the liquid water path by 10–20% and therefore the cloud opacity by 5–50%. These results show the potential of the new scheme to reduce the *too few, too bright* bias by increasing low-level CF and decreasing cloud reflectance.

1. Introduction

Clouds have a large impact on the radiative budget of the Earth and are the major source of spread in climate sensitivity estimates (Bony & Dufresne, 2005; Vial et al., 2013; Zelinka et al., 2017). Low-level clouds are ubiquitous over the globe and strongly impact shortwave (SW) radiative fluxes and, to a lesser extent, longwave (LW) radiative fluxes at the top of atmosphere. As a result, their representation in climate models is particularly critical. Many models share two compensating errors by underestimating low-level cloud fraction (CF) and overestimating reflectance (Nam et al., 2012; Zhang et al., 2005). Konsta et al. (2016) hypothetized that neglecting the vertical heterogeneity of cloud properties may partly explain this widespread model bias. Using large eddy simulations (LES), Neggers et al. (2011) found that neglecting the subgrid-scale (SGS) vertical heterogeneity of cumulus clouds resulted in biases of 50% to 100% on the top of atmosphere SW cloud radiative forcing. Del Genio et al. (1996) also pointed out that although the total water distribution can be used to estimate CF by volume CF_{vol} in a model grid box, radiative transfer schemes need as input the CF by surface CF_{surf}, that is, the surface of the grid box that is covered by clouds when looking from above. The difference between the two CF, by volume and by surface, is a way to characterize this vertical heterogeneity. Brooks et al. (2005) demonstrated using radar and lidar observations that the difference between the two can be significant and that CF_{surf} is typically greater than CF_{vol} by about 30%.

Boundary layer clouds are not explicitly resolved in general circulation model (GCM) and must be parameterized. A widely used family of cloudiness parameterization, referred to as statistical schemes, represents the SGS horizontal heterogeneity of total water content by a probability density function (PDF) (Mellor, 1977; Sommeria & Deardorff, 1977). In their general form, the following equations are used to compute the condensed water q_c and *CF*:

$$\begin{cases} s = a_l(q_t - q_{sat}(T_l)) \\ q_c = \int_0^{+\infty} s.P(s)\mathrm{d}s \\ CF = \int_0^{+\infty} P(s)\mathrm{d}s \end{cases} \quad (1)$$

where s is the water saturation deficit, a_l is a thermodynamic constant (see Appendix A1), q_t the total water (condensed q_c + vapor q_v), q_{sat} the saturation mixing ratio, T_l the liquid temperature (see Appendix A1), and P a PDF. Various PDF schemes have been proposed, from a uniform PDF (Le Treut & Li, 1991) to a unimodal lognormal (Bony & Emanuel, 2001), a beta (Tompkins, 2002), or a bi-Gaussian PDF (Jam et al., 2013). This last distribution (which is based on previous studies by Bogenschutz et al., 2010; Golaz et al., 2002; Larson et al., 2002, 2001; Lewellen & Yoh, 1993; Neggers, 2009; Perraud et al., 2011) aims at representing explicitly the bimodality in tropical water vapor distributions by introducing a moister mode that corresponds to boundary layer thermals and a drier mode that corresponds to the surrounding air (later called the *environment*). Some models try to explicitly connect this bi-Gaussian distribution to a mass flux representation of the boundary layer convection that splits the horizontal grid into updrafts and their environment (Neggers, 2009). It is the case of the LMDz GCM that couples the *thermal plumes* model of Rio et al. (2010) with the bi-Gaussian cloud scheme of Jam et al. (2013).

If the choice of a better PDF may improve the evaluation of the *CF* defined by equation (1), the problem mentioned by Del Genio et al. (1996) that stipulates that *CF* is calculated by volume but is directly used as a fraction defined by surface by the radiative code remains. Therefore, an implicit assumption of the models using the statistical schemes is that CF defined by volume and by surface are equal, which is far from what is observed (Brooks et al., 2005) or computed by LES models (Neggers et al., 2011).

In general, Pincus and Klein (2000) suggest that SGS water content heterogeneity is not only important in the assessment of CF by volume and by surface but also affects many other processes such as the interaction of clouds with radiation (Barker & Wielicki, 1997; Li et al., 2005) or autoconversion rates (Boutle et al., 2014; Kawai & Teixeira, 2012; Pincus & Klein, 2000). We choose here to focus on the computation of CF only, all things otherwise being equal, as the coupling with other processes deserves a dedicated study.

The aim of this study is therefore to develop a parameterization of the SGS water content heterogeneity in the SCM version of the LMDz GCM that allows the computation of (1) the CF by volume CF_{vol}, which is the CF computed over a layer of a given thickness Δz and (2) the CF by surface CF_{surf}, which is the projected cloud area. To develop and calibrate this parameterization in LMDz, we use LES simulations of boundary layer clouds. We have based our work on the LMDzβ6 version of LMDz, an improved version of LMDz5B presented in Hourdin et al. (2013).

In section 2, we present the methodology we follow to explore and constrain two parameterizations, which are then presented in detail in section 3: a first one that combines a vertical and a horizontal PDF (section 3.1) and a second one that is based on a single 3-D PDF (section 3.2). In section 4, we compare the two parameterizations to LES direct calculations in order to define the most accurate (section 4.1). We finally discuss the sensitivity to the vertical resolution (section 4.2) and explore the results of the SCM version of the LMDzβ6 GCM (section 4.3).

2. Methods and Models

2.1. Models and Test Cases

In order to develop and constrain the two parameterizations, we considered three test cases of shallow cumulus clouds that are represented in Figure 1.

The first case, ARM, represents the growing of the continental boundary layer on 21 June 1997 over the U.S. Southern Great Plains ARM site (Brown et al., 2002). It highlights the diurnal cycle of shallow convection over 15 hr, from 5h30 to 20h30 LT. Clouds appear at 9h30 LT and dissipate by 18h30 LT. The cloud base increases from 800 to 1,200 m and the cloud top from 1,100 to 2,700 m. This case has been for long recognized as representative of purely local continental shallow convection and used by many authors to develop shallow convection schemes (Bogenschutz et al., 2012; Cheng & Xu, 2015; Jam et al., 2013; Neggers et al., 2004; Rio & Hourdin, 2008). However, a recent study from Zhang et al. (2017) suggests that it is subject to some large-scale influence, with a relatively large surface latent heat flux compared to the values derived from the composite

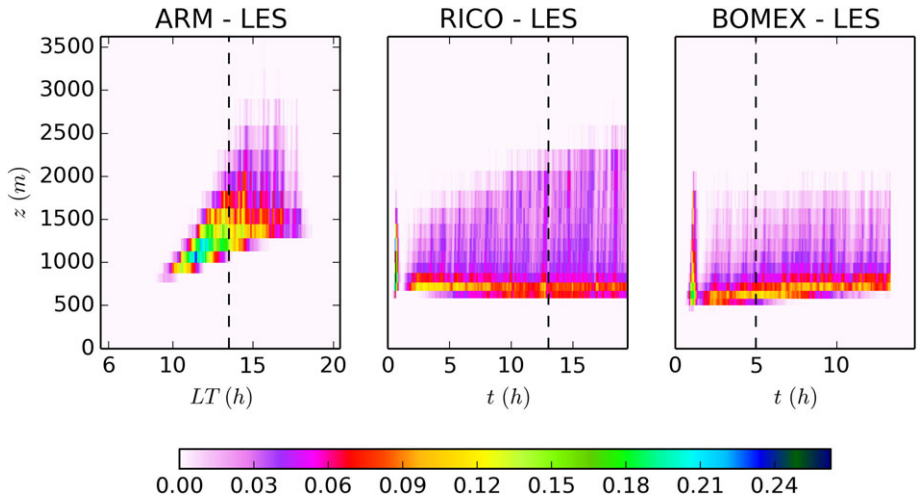

Figure 1. Time evolution of the cloud fraction vertical profiles for the ARM, RICO, and BOMEX LES simulations. The black dashed vertical lines show the times when vertical profiles are represented in the rest of the paper. Note that unlike the RICO and BOMEX cases that are quasi-stationary, the ARM case has a diurnal cycle and local time (LT) is therefore shown on the *x* axis. LES = large eddy simulation; BOMEX = Barbados Oceanographic Meteorological Experiment.

of all the cumulus days over more than 10 years. As our study aims at testing impacts of the SGS water content heterogeneity on low-level clouds and does not specifically focus on local surface-driven shallow convection processes, we kept working on this version of the ARM case.

The second case represents a field of rainy shallow cumulus clouds over the western Atlantic ocean, derived from the RICO campaign described in VanZanten et al. (2011). Clouds cover the whole duration of the simulation. The cloud base remains at the same level (∼500 m) and the cloud top increases from 1,000 to 2,500 m.

The last case represents an oceanic cloudy boundary layer derived from the Barbados Oceanographic Meteorological Experiment (BOMEX) and described in Siebesma et al. (2003). The cloud base and cloud top remain at the same level (∼500 and 2,000 m, respectively), and the simulation lasts 15 hr, which is longer than the 6-hr runs used for the LES intercomparison of Siebesma et al. (2003).

The three cases used here have been shown to reproduce observations (Brown et al., 2002; Siebesma et al., 2003; VanZanten et al., 2011), and our LES compare well with others from different intercomparison exercises.

LES are performed using the LES version of the nonhydrostatic model Meso-NH (Lac et al., 2018). In this model, a bulk one-moment microphysics scheme called the mixed ICE3 scheme (Caniaux et al., 1994; Pinty & Jabouille, 1998) is used to reproduce the different processes such as condensation, evaporation, precipitation, and autoconversion. It predicts the mass mixing ratio of five water species (among which only two, cloud droplets and raindrops, are present here) and is close to a Kessler scheme as far as warm clouds are concerned. An all-or-nothing cloud scheme is used assuming that any grid can only be either totally saturated or unsaturated, and no SGS condensation scheme is allowed. Although the computation of SGS CF could provide a better agreement with observations, especially in terms of cloud size, we decided not to use any SGS cloud scheme in the LES. Indeed, we want to ensure that clouds are explicitly resolved by the LES. The turbulence scheme uses a prognostic equation of the turbulent kinetic energy using a Deadorff mixing length scale (Cuxart et al., 2000).

To characterize the thermals, we use the conditional sampling presented in Couvreux et al. (2010). This sampling allows a continuous characterization of convective updrafts from the surface to the cloud tops. It uses the concentration in the atmosphere of a passive tracer emitted at the surface. The tracer is emitted homogeneously with a constant vertical flux and undergoes a radioactive decay of 15 mn. A LES grid point then belongs to a thermal if the following criteria are satisfied simultaneously: (a) the tracer concentration anomaly at this point is superior to the standard deviation of the tracer concentration at this level or to a minimum threshold, (b) its vertical velocity is positive, and (c) in the presence of clouds, the condensed water is nonnull in the three upper quarters of the cloud.

Finally, the domain size of all three LES shallow cumulus cloud cases is 6.4 km by 6.4 km, with a 4-km height and 25-m resolution in the three directions. Our domain is rather small compared to recent LES whose domain size reaches typically 10 km by 10 km and sometimes more. Therefore, our simulations tend to slightly overestimate CF by a few percent.

The SCM simulations are performed using LMDzβ6, an improved version of LMDz5B presented in Hourdin et al. (2013) and close to the new LMDz6 model. It runs with a time step of 10 mn, and we checked the sensitivity of our results to three different vertical resolutions (see Figure 14 in Appendix A2). As far as the radiative transfer scheme is concerned, the heating rates are prescribed at each level, independently from the different parameterizations we test. However, the radiative fluxes are computed for diagnostic purposes as we will see later in Figure 13. Further details relevant to this work are presented in the next section.

2.2. LMDz Boundary Layer and Cloudiness Parameterization

In the cloudy boundary layer turbulence occurs at various scales. Small-scale turbulence dominates the total vertical transport in the unstable surface layer while coherent structures as thermal plumes play a key role in the mixed layer. Observations show that in the cloudy boundary layer, the major part of vertical transport is carried out by those coherent structures and that cumulus clouds are the saturated part of these thermals (LeMone & Pennell, 1976).

In our model, the vertical SGS transport is obtained by modeling both the mass flux and small-scale turbulence. The mass flux scheme, called the *thermal plume* model (Rio & Hourdin, 2008), describes the nonlocal transport induced by the boundary layer thermals, whereas the small-scale turbulence is computed by a diffusivity model. The thermal plume model is coupled to a statistical cloud scheme based on a bi-Gaussian distribution of saturation deficit s (Jam et al., 2013) which can be written as follows:

$$P(s) = \alpha \frac{e^{-\frac{1}{2}\left(\frac{s-\bar{s}_{\text{th}}}{\sigma_{h_{\text{th}}}}\right)^2}}{\sigma_{h_{\text{th}}}\sqrt{2\pi}} + (1-\alpha)\frac{e^{-\frac{1}{2}\left(\frac{s-\bar{s}_{\text{env}}}{\sigma_{h_{\text{env}}}}\right)^2}}{\sigma_{h_{\text{env}}}\sqrt{2\pi}}, \tag{2}$$

where α is the fraction of the thermal plumes in the layer, $\bar{s}_{\text{th}}$ and $\bar{s}_{\text{env}}$ the mean values of the saturation deficits in the thermals and in the environment, respectively, and $\sigma_{h_{\text{th}}}$ and $\sigma_{h_{\text{env}}}$ the standard deviations of the distributions in the thermals and in the environment, respectively.

The LMDzβ6 statistical cloud scheme, based on this bi-Gaussian distribution of saturation deficit, is coupled to the mass flux scheme from Rio et al. (2010) that provides directly s_{th}, s_{env}, and α. The only variables of equation (2) that need to be parameterized are then the standard deviations $\sigma_{h_{\text{th}}}$ and $\sigma_{h_{\text{env}}}$. They control the SGS saturation deficit heterogeneity. This heterogeneity is mainly driven by the difference between the saturation deficit in the thermal plumes and that in their surrounding environment. The higher the difference, the higher the saturation deficit heterogeneity in these regions. For a given difference in saturation deficit between the plumes and the environment, $\sigma_{h_{\text{th}}}$ is expected to scale with the ratio of the lateral area of mixing to the volume of the thermal plumes. Let us call A the horizontal surface of any individual thermal plume and its surrounding environment. αA is the surface of this plume in this domain, and $(1-\alpha)A$ is the surface of the environment. The radius of the plume is $R = \sqrt{\frac{\alpha A}{\pi}}$, and its lateral mixing surface is $S = 2\pi\sqrt{\frac{\alpha A}{\pi}}\Delta z$. The volume of the plume is $V = \alpha A \Delta z$. Consequently, for a given contrast in the saturation deficit, $\sigma_{h_{\text{th}}}$ scales as $\frac{S}{V} = 2\sqrt{\frac{\pi}{\alpha A}}$ and $\sigma_{h_{\text{th}}} \propto \frac{1}{\sqrt{\alpha}}$. Applying the same reasoning to $\sigma_{h_{\text{env}}}$, we get $\sigma_{h_{\text{env}}} \propto \frac{\sqrt{\alpha}}{(1-\alpha)}$. This is why Jam et al. (2013) proposed that the standard deviations of the saturation deficits should take the following form:

$$\begin{cases} \sigma_{h_{\text{th}}} = c_{\text{th}} \frac{1}{\sqrt{\alpha}}(\bar{s}_{\text{th}} - \bar{s}_{\text{env}}) + b\bar{q}_{t\,\text{th}} \\ \sigma_{h_{\text{env}}} = c_{\text{env}} \frac{\sqrt{\alpha}}{1-\alpha}(\bar{s}_{\text{th}} - \bar{s}_{\text{env}}) + b\bar{q}_{t\,\text{env}}, \end{cases} \tag{3}$$

where c_{th}, c_{env}, and b are tunable parameters.

The ARM and BOMEX cases were used as a basis for the calibration of this parameterization. The LES have been postprocessed using the conditional sampling presented above. The five parameters of the bi-Gaussian PDF ($\bar{s}_{\text{th}}$, $\bar{s}_{\text{env}}$, $\sigma_{h_{\text{th}}}$, $\sigma_{h_{\text{env}}}$, and α) were calculated at each LES level, thus creating PDFs that represent the horizontal heterogeneity in the LES. The same was done in each SCM layer on the LMDzβ6 vertical discretization (red dots in Figure 14), and the SCM vertical profiles of $\sigma_{h_{\text{th}}}$ and $\sigma_{h_{\text{env}}}$ (equation (3)) were then adjusted to the LES

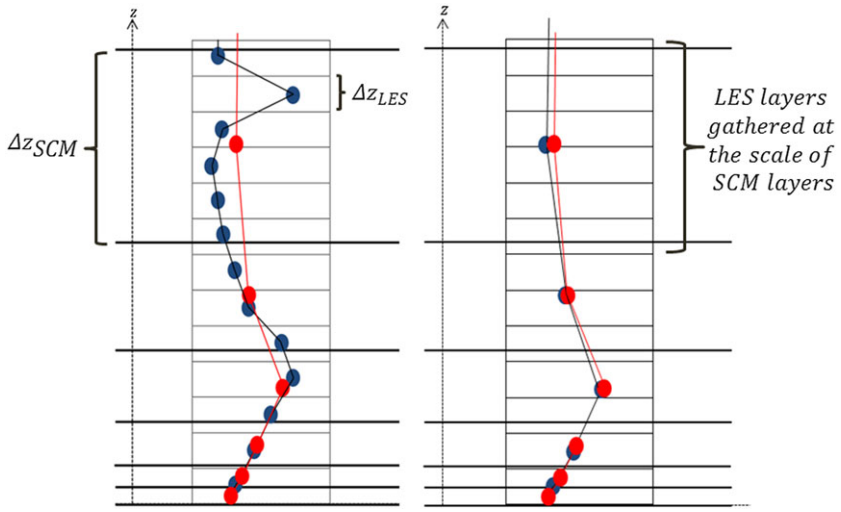

Figure 2. Idealized vertical profiles of $\sigma_{h_{env}}$ on different vertical grids. (left) Blue dots are obtained with LES data on the LES-refined vertical grid (Δz_{LES} = 25 m); red dots are obtained with SCM data on the SCM LMDzβ6 vertical grid ($\Delta z_{SCM} \in$ [20;150 m] here). This panel shows how the SCM vertical profile of $\sigma_{h_{env}}$ is compared to the LES one in Jam et al. (2013) when tuning the c_{env} and b coefficients. (Right) Blue dots are obtained by gathering LES levels to match the SCM ones, so that the tuning process is based on quantities computed on the same scale. LES = large eddy simulations; SCM = single column model.

vertical profiles by adjusting the tunable parameters c_{th} , c_{env}, and b (Figure 2, left). The PDFs obtained in the SCM then represent the horizontal SGS saturation deficit heterogeneities of each SCM layer. This tuning process can present a discrepancy because the SCM vertical profiles of $\sigma_{h_{th}}$ and $\sigma_{h_{env}}$ are not evaluated on the same vertical grid as the LES vertical profiles (Figure 2, left). To solve this discrepancy, we tune the model by gathering data on multiple LES levels to match the SCM levels, as shown in Figure 2.

3. Including Vertical SGS Heterogeneity of CF

In sections 3 to section 4.2, we use LES only to explore parameterizations; even if as shown in the right panel of Figure 2, we will often alter the LES vertical resolution to match the SCM one.

To develop a parameterization of cloudiness that accounts for vertical heterogeneity of water content at a subgrid scale, we consider different options. The first option consists in combining a vertical PDF of saturation deficit s to the horizontal one of Jam et al. (2013), thereby assuming that the vertical and the horizontal SGS heterogeneities are statistically independent. The second option is to create a PDF of saturation deficit directly based on 3-D statistics of LES data gathered at the scale of the SCM grid boxes (Figure 2, right) and then to parameterize CF_{surf} from CF_{vol}. In sections 3.1 and 3.2, we will present and discuss the results obtained using these two methods.

3.1. Method 1: Combining a Vertical PDF With the Horizontal PDF

In equation (1) that define condensed water and CF in the cloudiness parameterization, it is implicitly assumed that $s(x, y, z) = s(x, y)$. Said differently, it is assumed that the saturation deficit has a constant value along the vertical axis at a SCM subgrid scale, that is, that clouds homogeneously fill the layers vertically (as mentioned in Del Genio et al., 1996). We therefore introduce the saturation deficit $\bar{s}_z(x, y)$ which is vertically averaged over each layer of thickness Δz and rewrite equation (1) as follows:

$$\begin{cases} \bar{s}_z(x,y) = \frac{1}{\Delta z} \int_{\Delta z} s(x,y,z)\mathrm{d}z \\ q_c = \int_{\bar{s}_z=0}^{\bar{s}_z\to+\infty} \bar{s}_z . P(\bar{s}_z)\mathrm{d}\bar{s}_z \\ CF = \int_{\bar{s}_z=0}^{\bar{s}_z\to+\infty} P(\bar{s}_z)\mathrm{d}\bar{s}_z \end{cases} \quad (4)$$

To illustrate our method, we show in Figure 3 a layer whose size is typical of a SCM and which is filled by three different rearrangements of the same LES results. The top panel shows the real cloud organization of

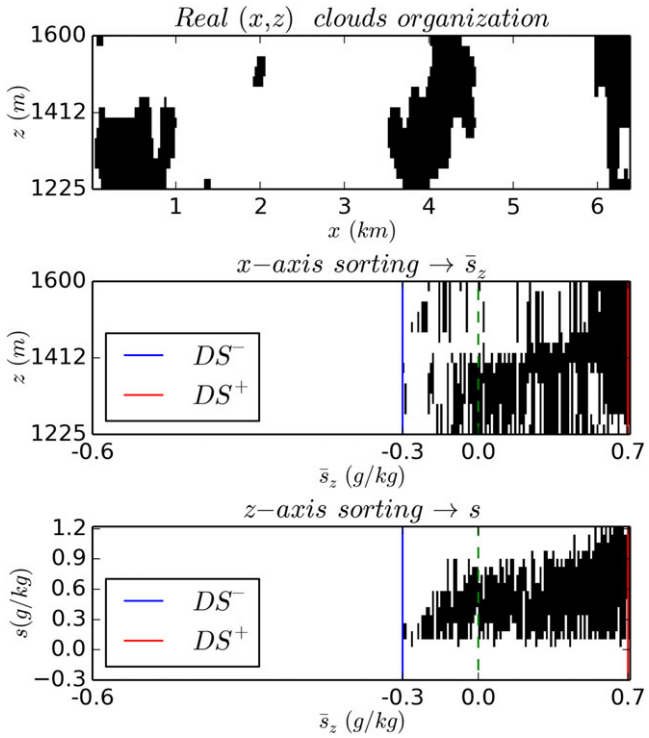

Figure 3. Vertical cross section of cloudy points (in black) in a large eddy simulations (LES) domain whose size is typical of single column model simulations. (top) LES cloud scene, for which $CF_{vol} = 0.22$ and $CF_{surf} = 0.42$. (middle) Rearrangement of the LES cloud scene by sorting the horizontal x axis in order of increasing $\bar{s}_z$. (bottom) Sorting of the vertical z axis by order of increasing saturation deficit s. The three cloud scenes are statistically equivalent for a general circulation model. The parameters DS^- and DS^+ show the limits of the transition zone from fully clear to fully cloudy conditions over the vertical at a subgrid scale. Data from the LES of the ARM case at 13h30 LT.

this layer. We rearrange it by first sorting the horizontal xy coordinates (only the x coordinate is represented here) by order of increasing $\bar{s}_z$ (the vertically averaged saturation deficit; see the middle panel of Figure 3). We then rearrange it by sorting the vertical z coordinate by order of increasing saturation deficit s (bottow panel). The cloud scene shown in the bottom panel is, statistically speaking, the same as the one in the top panel for the SCM, because no geometry exists at a subgrid scale. That statistical rearrangement reveals a parameter $DS = DS^+ - DS^-$ that highlights the transition from fully clear to fully cloudy conditions due to the vertical sublayer heterogeneity. Indeed, for $\bar{s}_z \leqslant DS^-$, no clouds are present, and for $\bar{s}_z \geqslant DS^+$, the vertical layer is entirely filled by clouds. We also note that in the bottom panel, clouds are present over a significant interval of negative $\bar{s}_z$ values, between $\bar{s}_z = DS^-$ and $\bar{s}_z = 0$. This interval where clouds are present for negative values of $\bar{s}_z$ is not taken into account in the calculation of CF by equation (4).

Knowing that, we introduce Q_{vol}, the normalized PDFs of $s(x, y, z)$ along the vertical axis inside a SCM layer, so we can make a variable change and replace the integral over the layer volume by an integral over s. Note that $\int_{s\to-\infty}^{s\to+\infty} Q_{vol}(s)ds = 1$. We also introduce a Heaviside function $\mathcal{H}(\bar{s}_z > 0)$ to rewrite the limits of the integrals over $\bar{s}_z$ in the expressions of q_c and CF. Equation (4) then become as follows:

$$\begin{cases} \bar{s}_z = \int_{s\to-\infty}^{s\to+\infty} s.Q_{vol}(s)ds \\ q_c = \int_{\bar{s}_z\to-\infty}^{\bar{s}_z\to+\infty} \mathcal{H}(\bar{s}_z > 0) \left(\int_{s\to-\infty}^{s\to+\infty} s.Q_{vol}(s)ds \right) P(\bar{s}_z)d\bar{s}_z \\ CF = \int_{\bar{s}_z\to-\infty}^{\bar{s}_z\to+\infty} \mathcal{H}(\bar{s}_z > 0) \left(\int_{s\to-\infty}^{s\to+\infty} Q_{vol}(s)ds \right) P(\bar{s}_z)d\bar{s}_z \end{cases} \quad (5)$$

Here the saturation deficit has not the same value along the vertical axis at a subgrid scale anymore, and the condition $\bar{s}_z(x, y) > 0$ used as condensation threshold should be replaced by $s(x, y, z) > 0$. The Heaviside function relevant for our approach is then $\mathcal{H}(s > 0)$ instead of $\mathcal{H}(\bar{s}_z > 0)$ and should be placed inside the integral over s in the expression of q_c. The equation can then be simplified by removing the Heaviside function and setting the lower bound of the integral to 0. As for the CF, we introduce the difference between CF_{vol} and CF_{surf}. For the CF by volume CF_{vol}, we follow the same steps as for the condensed water q_c, add $\mathcal{H}(s > 0)$ inside the integral over s, and then remove it by changing the bound to $s = 0$. For the CF by surface CF_{surf}, we introduce the following:

$$Q_{surf}(\bar{s}_z) = \mathcal{H}\left(\int_{s=0}^{s\to\infty} Q_{vol}(s)ds > 0 \right) \quad (6)$$

This formulation accounts for every condensate that is present in the vertical of a subcolumn in the calculation of CF_{surf}, even if $\bar{s}_z < 0$ in this subcolumn. The final expressions of condensed water and CF at a subgrid scale can then be summarized as follows:

$$\begin{cases} q_c = \int_{\bar{s}_z\to-\infty}^{\bar{s}_z\to+\infty} \left(\int_{s=0}^{s\to+\infty} s.Q_{vol}(s)ds \right) P(\bar{s}_z)d\bar{s}_z \\ CF_{vol} = \int_{\bar{s}_z\to-\infty}^{\bar{s}_z\to+\infty} \left(\int_{s=0}^{s\to+\infty} Q_{vol}(s)ds \right) P(\bar{s}_z)d\bar{s}_z \\ CF_{surf} = \int_{\bar{s}_z\to-\infty}^{\bar{s}_z\to+\infty} Q_{surf}(\bar{s}_z)P(\bar{s}_z)d\bar{s}_z, \end{cases} \quad (7)$$

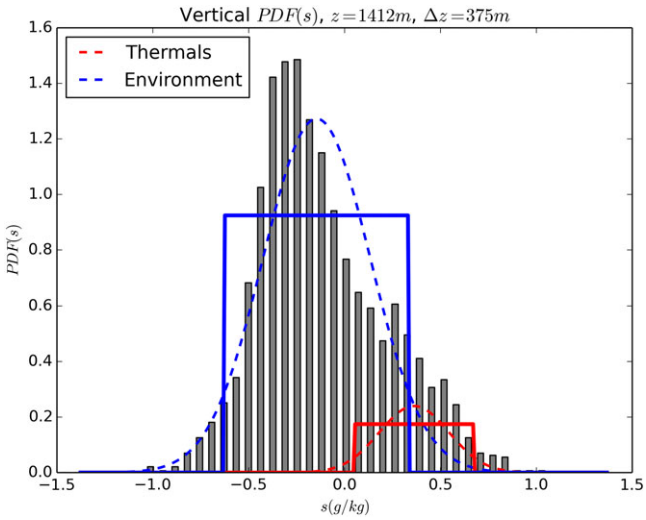

Figure 4. Gray bars: 1-D histograms of saturation deficit s, obtained from each LES subcolumns for which $\bar{s}_z \in [DS^-; DS^+]$ (see Figure 3). The colored lines represent different vertical PDFs Q_{vol}, estimated by different fits of this histogram. The vertical PDFs are sampled in thermal plumes and environment regions according to Couvreux et al. (2010). Red lines fit the thermal regions with squared (solid line) or Gaussian (dashed line) distributions. Blue lines fit the environment regions with squared (solid line) or Gaussian (dashed line) distributions. Data come from the LES of the ARM case at 13H30 LT. We create SGS heterogeneity by weighting on the horizontal PDF of Jam et al. (2013) with the vertical PDF. LES = large eddy simulations; PDF = probability density function; SGS = subgrid scale.

where s is the saturation deficit, $\bar{s}_z$ the SCM SGS vertically averaged saturation deficit, P the horizontal PDF, and Q_{surf} and Q_{vol} the vertical PDFs. The integral over $\bar{s}_z$ is done from $-\infty$ to $+\infty$ as negative values of $\bar{s}_z$ do not strictly imply that s is negative throughout the LES subcolumns. Indeed, as mentioned just above, we observe in Figure 3 unsaturated columns ($\bar{s}_z < 0$) that are nevertheless partially cloudy ($s > 0$). The integral over s is done from 0 to $+\infty$ in order to gather positive values of saturation deficit in the calculations of condensed water or CF. We also introduce the indices *vol* and *surf* now that the distinction between CF by volume and CF by surface explicitly exists in the cloudiness parameterization. The radiative transfer code that computes the vertical LW and SW fluxes will use the CF by surface CF_{surf}, whereas the physical parameterizations that compute 3-D mass fluxes and cloud physical properties will use the CF by volume CF_{vol}. In these equations the SGS total heterogeneity is the product of the vertical and horizontal SGS heterogeneities considered independently.

Our method presents similarities with the parameterization of Larson and Schanen (2013) that links specific points in the horizontal SGS PDFs of hydrometeors at multiple levels through vertical profiles. However, this study does not refer to vertical heterogeneity at a subgrid scale and only focuses on it at multiple vertical levels.

3.1.1. Evaluation of the Vertical PDFs Q_{vol} and Q_{surf} Using LES Data

To evaluate the shape of Q_{vol} and Q_{surf}, we use the LES layers gathered to match the SCM ones and calculate vertical distributions of saturation deficit $s(x, y, z)$. We only consider verticals for which $\bar{s}_z \in [DS^-; DS^+]$, which corresponds to the interval for which the LES subcolumns are either totally covered or completely cloud free but partially covered (Figure 3, bottom). The 1-D histogram in Figure 4 displays the values of s for each grid points of each subcolumns for which $\bar{s}_z \in [DS^-; DS^+]$. This 1-D histogram is then a representation of the vertical SGS heterogeneity of saturation deficit in the SCM-like layer. The vertical PDF Q_{vol} is a fit of this 1-D histogram. To be consistent with Jam et al. (2013), we split the distribution into two normal distributions that correspond to the thermal and environment regions, as we do for the horizontal PDF and following the same conditional sampling of Couvreux et al. (2010). The PDF could be approximated by a Bi-Gaussian distribution. However, to allow the analytical calculation of Q_{vol}, we choose to approximate this vertical PDF by two uniform distributions centered on $\bar{s}_{th}$ and $\bar{s}_{env}$, with standard deviations $\sigma_{z_{th}}$ and $\sigma_{z_{env}}$. The spans of these uniform distributions are $\Delta s_{th} = \sqrt{12}.\sigma_{z_{th}}$ and $\Delta s_{env} = \sqrt{12}.\sigma_{z_{env}}$, and the functions Q_{vol} and Q_{surf} mentioned earlier

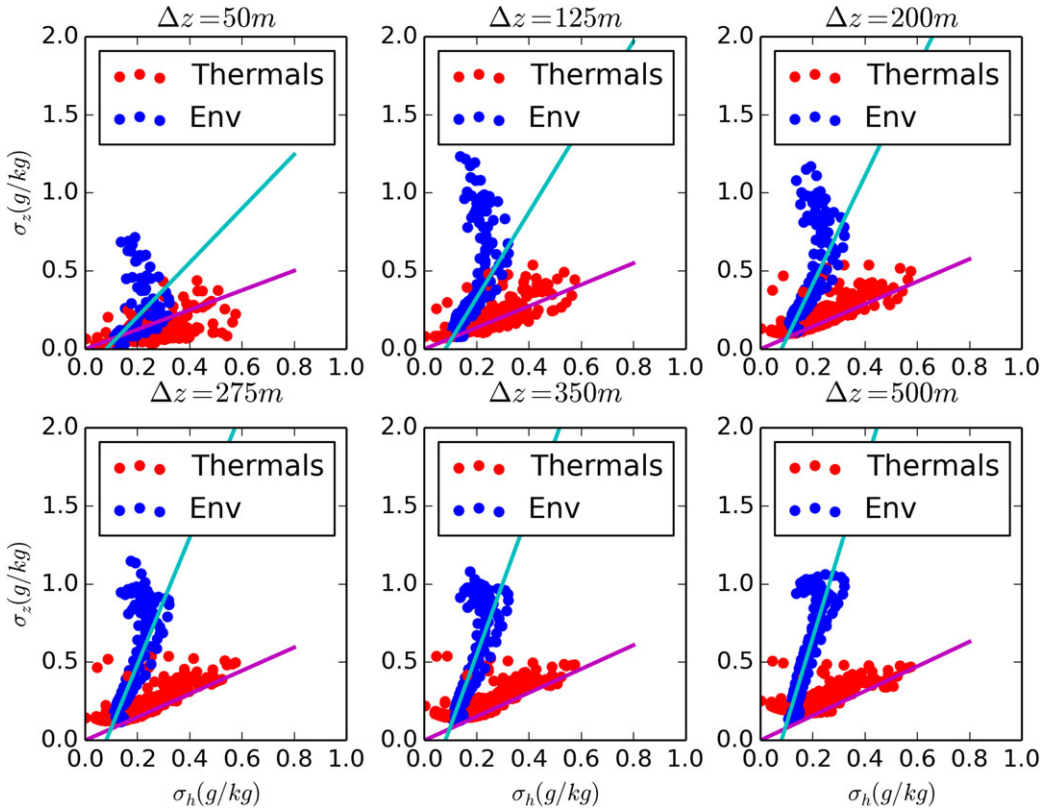

Figure 5. Scatter plots of the standard deviations $\sigma_{z_{th}}$ and $\sigma_{z_{env}}$ of the vertical distributions against the standard deviations $\sigma_{h_{th}}$ and $\sigma_{h_{env}}$ of the horizontal distributions, plotted for six different layer thicknesses $\Delta z \in [50;500\ \text{m}]$. Purple and cyan lines are the linear fits we propose for the thermal and environment regions, respectively (see equation (9)). Data originate from the large eddy simulations of the Barbados Oceanographic Meteorological Experiment case over the whole duration of the simulation.

then take the following form:

$$\begin{cases} Q_{\text{vol}}(s) = \alpha Q_{v_{th}}(s) + (1-\alpha)\, Q_{v_{env}}(s) \\ Q_{v_{\text{th,env}}}(s) = \begin{cases} 0 & \text{if } s \le \left(\bar{s}_z - \frac{\Delta s_{\text{th,env}}}{2}\right) \\ \frac{1}{\sqrt{12}.\sigma_{z_{\text{th,env}}}} & \text{if } \left(\bar{s}_z - \frac{\Delta s_{\text{th,env}}}{2}\right) \le s \le \left(\bar{s}_z + \frac{\Delta s_{\text{th,env}}}{2}\right) \\ 0 & \text{if } \left(\bar{s}_z + \frac{\Delta s_{\text{th,env}}}{2}\right) \le s \end{cases} \\ Q_{\text{surf}}\left(\bar{s}_z\right) = \mathcal{H}\left(\bar{s}_z > -\frac{\Delta s_{\text{env}}}{2}\right) \end{cases} \tag{8}$$

where $\mathcal{H}$ is the Heaviside function. It is worth reminding that parameterizing Q_{surf} using a Heaviside function that starts from $\bar{s}_z = -\frac{\Delta s_{\text{env}}}{2} = -\sqrt{3}.\sigma_{z_{\text{env}}}$ accounts for the fact that as far as radiation is concerned, any condensate on a vertical sublayer axis is considered as a cloud that should increase CF_{surf}, even when $\bar{s}_z \le 0$.

The standard deviation $\sigma_{z_{env}}$ and $\sigma_{z_{th}}$ now need to be parameterized and implemented in a GCM. Figure 5 shows the relation that exists between the horizontal and vertical standard deviations in the LES for SCM-like layers of thickness Δz. The linear fits that we propose for $\sigma_{z_{\text{th,env}}}$ based on the values of $\sigma_{h_{\text{th,env}}}$ (see Figure 5) are as follows:

$$\begin{cases} \sigma_{z_{th}} = 0.8 \left(\frac{\Delta z}{150}\right)^{0.1} \sigma_{h_{th}} \\ \sigma_{z_{env}} = 3. \left(\frac{\Delta z}{150}\right)^{0.5} \sigma_{h_{env}} - 0.08 \left(3. \left(\frac{\Delta z}{150}\right)^{0.5}\right) \end{cases} \tag{9}$$

Figure 5 also shows that the fits for the environment regions are not valid in all configurations. Typically, we can see that for $\Delta z = 125$ m, this parameterization underestimates the value of $\sigma_{z_{env}}$ by a factor of 2 in some

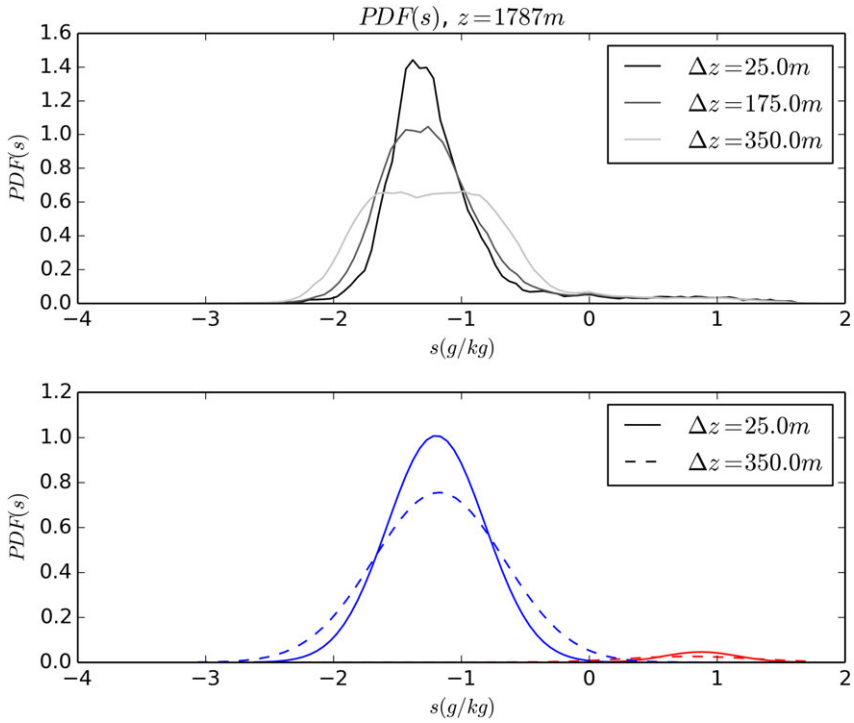

Figure 6. The 1-D histograms (top) and *PDFs* (bottom) of the 3-D distributions of saturation deficit *s* in SCM-like layers, with thicknesses varying from $\Delta z = \Delta z_{LES} = 25$ m (1 LES layer) to $\Delta z = 350$ m (14 LES layers). All the SCM-like layers are centered on the same median altitude. In the top plot, thermals and their environment are not distinguished. In the bottom plot, red lines represent a Gaussian fit of the PDFs of the thermals and blue lines of the environment, for different layer thicknesses Δz. Data originate from the LES of the ARM case at 13h30 LT. PDF = probability density function; SCM = single column model; LES = large eddy simulations.

grid boxes where $\sigma_{h_{env}} = 0.2$. These regions where $\sigma_{z_{env}} \geq 0.6$ mainly correspond to grid boxes located above the top of the clouds. In these boxes the thermal fraction is often close to zero, which tends to reduce the horizontal SGS heterogeneity $\sigma_{h_{env}}$ (see equation (3)), whereas the vertical SGS heterogeneity is still significant. Equations (2), (8), and (9) are used to solve equation (7) of the condensed water and CF calculated by volume and by surface. The detailed solution of this set of equations, as implemented in LMDzβ6, is described in Appendix A3.

3.2. Method 2: Considering Directly a 3-D PDF

We now present the second parameterization that consists in creating a PDF of saturation deficit *s* directly from the 3-D statistics of LES data gathered at the scale of a SCM grid box (see Figure 2, right) in order to establish a relationship between CF_{vol} and CF_{surf}.

Figure 6 shows some examples of PDFs of saturation deficit *s* obtained using LES data gathered at the scale of layers of different thicknesses Δz but at the same median altitude. As we can see, a change in the thickness Δz leads to some changes in the PDFs. If the mean values $\bar{s}_{th}$ and $\bar{s}_{env}$ do not change much when Δz changes, the standard deviations σ_{th} and σ_{env}, on the other hand, tend to increase as Δz increases. A slightly regular vertical gradient of σ_{th} and σ_{env} at these vertical scales may explain this behavior. Thicker layers contain air from more various regions, which tends to slightly increase the dispersion of *s* without necessarily changing $\bar{s}_{th}$ and $\bar{s}_{env}$. To take into account the thickness Δz of the layers, we thus decide to model the PDF as follows.

3.2.1. CF by Volume and Condensed Water

We keep the bi-Gaussian model proposed by Jam et al. (2013) and its approximation of the plumes as vertical cylinders. We neglect the thinning of the plumes within SCM-like layers and thus consider that the thermal plumes fraction α does not change with the layer thickness Δz. As suggested by Figure 6 we also consider that the mean values $\bar{s}_{th}$ and $\bar{s}_{env}$ do not change with Δz. However, we take into account the variations of the standard deviations σ_{th} and σ_{env} of the PDF with the layer thickness. To do so, we adapt equation (3) by introducing a dependency on the thickness of the layer in the parameters c_{th} and c_{env}.

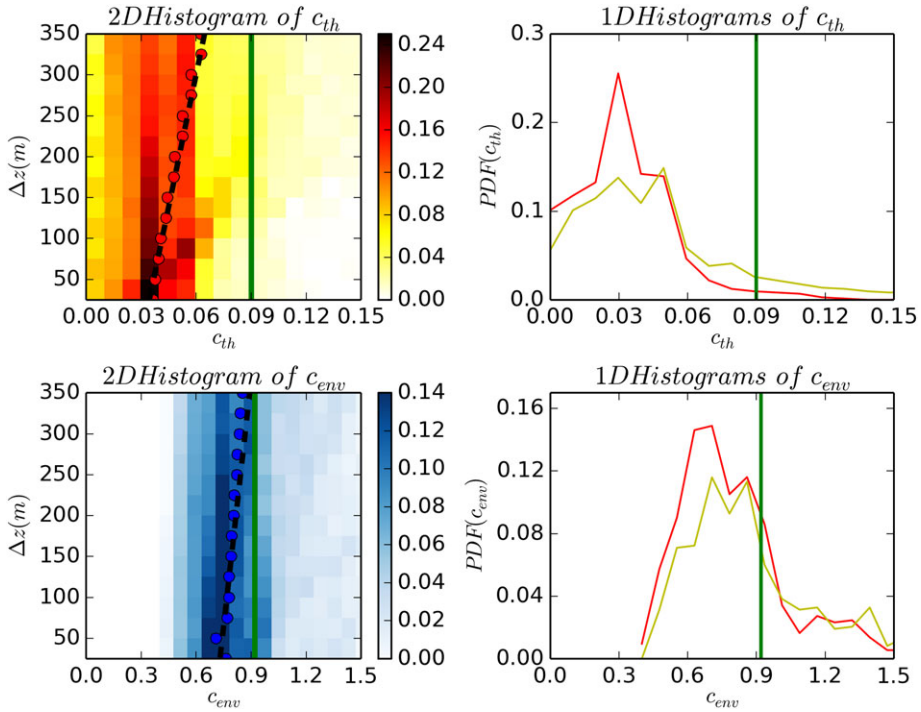

Figure 7. Left panel: 2D Histograms of the frequencies of occurrence of the coefficients c_{th} (top) and c_{env} (bottom) as computed using equation (3) in SCM-like layers of thicknesses Δz. Red and blue dots are the mean values of the histograms for each Δz. Black dashed lines represent the least squares linear fits of these dots and green solid lines are the constant values from Jam et al. (2013): $c_{th_{Jam}} = 0.09$ and $c_{env_{Jam}} = 0.92$. Right panel: 1D version of these histograms plotted for the extremes values $\Delta z = 25m$ (red lines) and $\Delta z = 350m$ (yellow lines). Data originate from the LES of the ARM, RICO and BOMEX cases at all times and altitudes from cloud bases to cloud tops.

To determine this dependency, we evaluate the standard deviations σ_{th} and σ_{env} in the LES data of our three test cases ARM, RICO, and BOMEX at all times and altitudes from cloud bases to cloud tops in layers of different thicknesses Δz and use it to retune the parameters c_{th} and c_{env} from equation (3). Figure 7 shows the 2-D histograms of the frequencies of occurrence of these tuned coefficients c_{th} and c_{env} for different thicknesses Δz. The least squares linear fits are given in equation (10). An increase in the layer thickness from $\Delta z = 25$ m (LES scale) to $\Delta z = 350$ m (SCM scale) results in a SGS dispersion 88% higher in the thermals and 22% higher in the environment.

$$\begin{cases} c_{\text{th}}(\Delta z) = 0.032 + 9.3 * 10^{-5}\Delta z \\ c_{\text{env}}(\Delta z) = 0.718 + 4.98 * 10^{-4}\Delta z \end{cases} \tag{10}$$

To compute the CF by volume CF_{vol} and the condensed water q_c using this parameterization, we rely on the sets of equations (1), (2), and (3) and on the adjusted coefficients c_{th} and c_{env} from equation (10).

3.2.2. CF by Surface

The other important feature that needs to be parameterized is the CF calculated by surface CF_{surf}. Neggers et al. (2011) proposed a parameterization of this CF by surface by weighting the CF by volume by a coefficient that depends only on the layer thickness Δz:

$$CF_{\text{surf}} = CF_{\text{vol}}(1 + \beta.\Delta z) \tag{11}$$

where $\beta = 0.0064$ m^{-1} has been estimated from a calibration on their LES results on the BOMEX case. This value depends on atmospheric conditions and has been found to vary in the range [0.0039 m^{-1}; 0.0480 m^{-1}] for the different tested cases (see Table 2 from Neggers et al., 2011). To implement this parameterization in the LMDzβ6 GCM, we follow the same method and gather results from different test cases. We group LES layers to obtain SCM-like grid boxes and compute the inverse of the overlap ratio: $\frac{1}{\rho} = \frac{CF_{\text{surf}}}{CF_{\text{vol}}}$ for each $\Delta z \in$ [25 m; 350 m] at various times and altitudes where clouds appear, typically between $z = 400$ m and $z = 2,200$ m. We plot in Figure 8 the 2-D histograms of frequencies of occurrence of ρ and $\frac{1}{\rho}$ for layers of different thicknesses

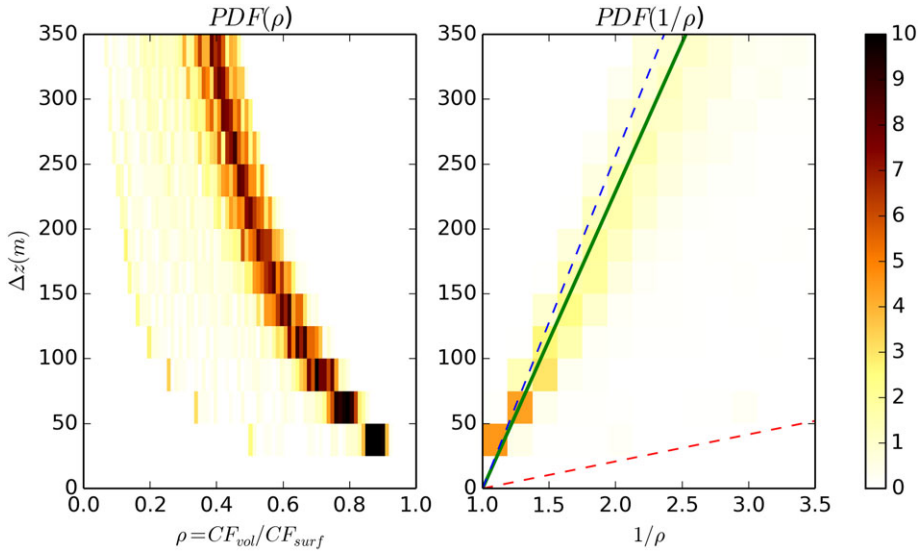

Figure 8. The 2-D histograms of the frequencies of occurrence of the overlap ratio $\rho = \frac{CF_{vol}}{CF_{surf}}$ (left) and of $\frac{1}{\rho}$ (right) in SCM-like layers of thicknesses Δz. Data originate from the LES of the ARM, RICO, and BOMEX cases at all times of the simulations. The solid green line represents the least squares fit of the function $\frac{1}{\rho} = (1 + \beta.\Delta z)$. The dashed blue and red lines are the fits using the lowest and highest values of β found by Neggers et al., 2011 (2011; $\beta = 0.0039$ m^{-1} and $\beta = 0.0480$ m^{-1}, respectively). SCM = single column model; LES = large eddy simulations; BOMEX = Barbados Oceanographic Meteorological Experiment.

Δz. The least squares fits that we show in this figure are obtained for $\Delta z \leq 350$ m, which correspond to typical values of layer thicknesses in current GCMs. The slope of the solid green line shown in Figure 8 is $\beta = 0.0044$ m^{-1}. We may note that this value, obtained by gathering data from the whole of the LES data set (ARM, RICO, and BOMEX), is in the range [0.0039 m^{-1}; 0.0480 m^{-1}] presented in Table 2 of Neggers et al. (2011). It shows a certain consistency between the results of the two studies. Our value of β is quite low in this range, which might be partly explained by its dependency to the vertical resolution: we use LES with a less refined vertical grid than that of the control grid from Neggers et al. (2011). This tends to decrease β ($\Delta z_{\text{LES}} = 25$ m in our case, whereas $\Delta z_{\text{LES,Neggers}} = 10$ m).

Note that in some cases, clouds might fill an entire SCM-like grid box ($CF_{\text{vol}} = 1$). This parameterization would then estimate $CF_{\text{surf}} > 1$ which is absurd. To address that problem, we specifically impose $CF_{\text{surf}} \leqslant 1$.

4. Discussion

In this section we first compare the two parameterizations introduced in section 3 using LES data only, in order to determine which is the most suitable for an implementation in the LMDzβ6 SCM. Second, we assess the results we obtain using the best parameterization when it is implemented in the LMDzβ6 SCM. In the rest of the paper, the first parameterization from section 3.1, in which we combine a vertical PDF and a horizontal PDF, is referred to as *Method 1*. The second parameterization from section 3.2, in which we create a 3-D PDF and parameterize CF_{surf} from CF_{vol}, is referred to as *Method 2*.

4.1. Comparison of the Two Parameterizations

Figure 9 shows the CF by volume CF_{vol} and CF_{surf} obtained using the two parameterizations presented in the previous sections as well as by direct calculations. These plots are based on LES data only, gathered at the scale of the LMDzβ6 SCM grid boxes. We display vertical profiles of the CF at the times shown in Figure 1 by red lines. Method 1 shows a good ability to reproduce the CF by volume on the RICO and BOMEX cases. The main features on these curves are the following: the cloud bases and the maximum of CF appear at the right altitudes, and the vertical profiles generally match the LES profiles. For the ARM case, however, this parameterization largely overestimate CF. It may come from the parameterization we chose for $\sigma_{z_{\text{env}}}$ (section 3.1). We may see in Figure 5 that the linear fit is valid for the BOMEX case. The fit for the RICO case is extremely similar (the slope differs by 4%, not shown) whereas the fit for the ARM case is quite different, typically showing a slope twice as large (not shown). The parameterization we propose then overestimates $\sigma_{z_{\text{env}}}$ for the ARM

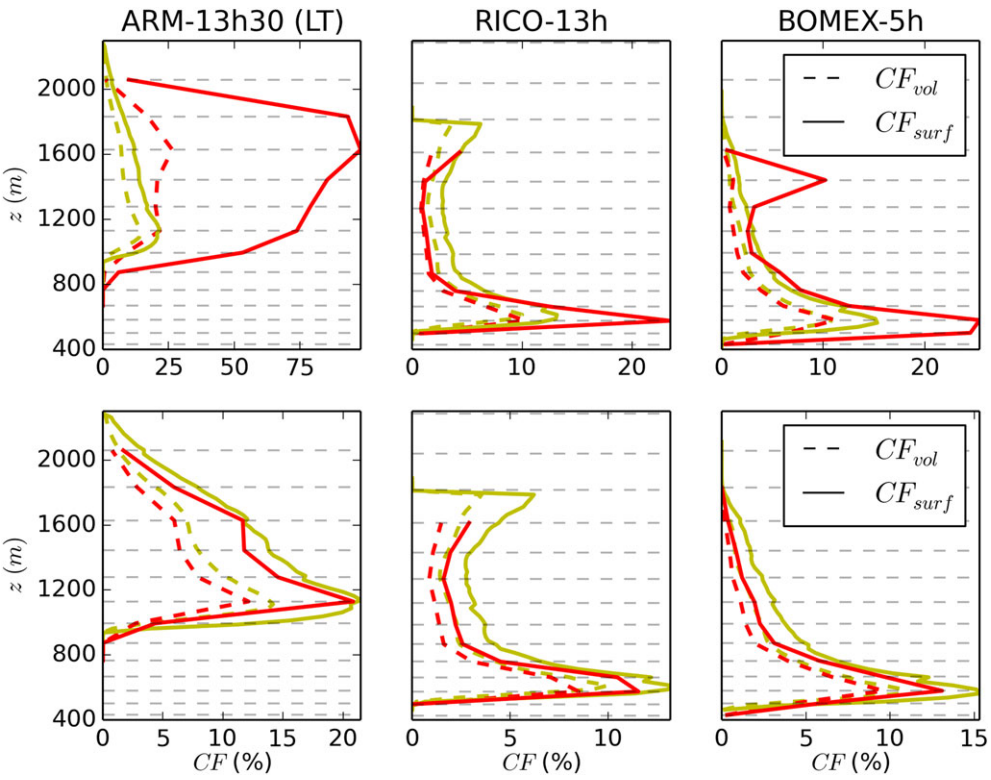

Figure 9. Vertical profiles of the cloud fractions CF_{vol} (dashed lines) and CF_{surf} (solid lines) obtained with LES data gathered at the scale of the LMDz6 SCM grid boxes. Yellow lines represent the direct calculations of the cloud fractions in the LES and red lines the parameterization of the cloud fractions. First row: Method 1. Second row: Method 2. The second parameterization shows the best results and is therefore the focus of our discussion.

case, which directly impacts on the CF_{vol}. On the same Figure 9, CF_{surf} shows two other discrepancies. While the large overestimation for the ARM case can be explained by the previous explanations, the fractions for the RICO and BOMEX cases are well estimated except on specific altitudes close to the cloud bases (RICO and BOMEX, 600 m) and just below the cloud top (BOMEX, 1,500 m). At these altitudes, the horizontal PDF naturally widens due to the mixing in one layer of wet air from the clouds and dry air from the surrounding environment. This increases the horizontal standard deviation. Method 1 then computes too large vertical standard deviations leading to an overestimation of the CF. To conclude on this parameterization, the assumption we made that horizontal and vertical saturation deficit standard deviations $\sigma_{h_{th,env}}$ and $\sigma_{z_{th,env}}$ are directly proportional seems to be too strong. Therefore, the sensitivity to the coefficients we introduce makes it difficult to tune the parameterization for all cases.

Method 2 shows less biases. Two important features appear on Figure 9. First, all the cloud bases and tops are simulated at the right altitudes. Second, all the CF by volume and by surface reproduce accurately the vertical profiles even though the parameterization slightly underestimates their values. This parameterization does not introduce large biases as the Method 1 does when the atmosphere presents strong vertical SGS gradients that are uncorrelated with horizontal SGS heterogeneity. Therefore, we focus on Method 2 in the rest of the discussion.

4.2. Sensitivity to the Vertical Discretization

Figure 10 shows the estimated errors made by Method 2 on the CF_{vol}, CF_{surf} and on the condensed water q_c for different vertical grids. We used LES data only, gathered at the scale of the three vertical discretizations presented in Figure 14. All the other parameters of this parameterization remain unchanged. The model slightly underestimates the CF by volume by 1 to 2 percent, the CF by surface by 1 to 5 percent, and the condensed water by up to $7.10^{-3}(g/kg)$, quasi independently of the vertical grid. The Root Mean Squared Error (RMSE) calculated as $RMSE = \sqrt{\frac{1}{n}\sum_{i=0}^{n}\left(X(i) - X_{param}(i)\right)^2}$ with $X \in [CF_{vol}, CF_{surf}, q_c]$, is then not systematically improved

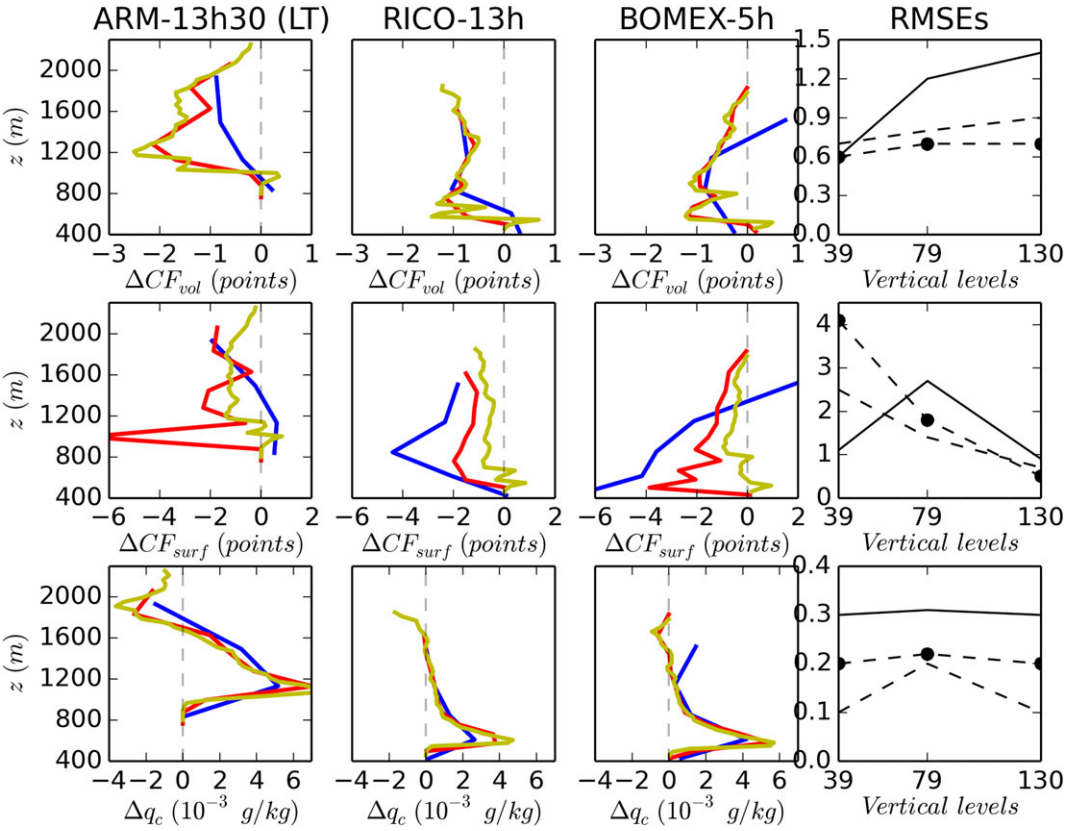

Figure 10. Sensitivity of layer properties to the vertical resolution: differences between the cloud fractions by volume CF_{vol} (first row), the cloud fractions by surface CF_{surf} (second row), and the condensed water q_c (third row) obtained by direct calculation and using Method 2 from LES data gathered at the scale of SCM grid boxes. Blue, red, and yellow lines show the calculations on the LMDz5B 39 levels, LMDzβ6 79 levels, and LMDzβ6 130 levels vertical grids, respectively. The right column represents the RMSE of CF_{vol} (first row), of CF_{surf} (second row), and of q_c (third row) as functions of the three vertical grids. Solid lines represent the RMSE for the ARM case, dashed lines for the RICO case, and dash-dotted lines for the BOMEX case. The parameterization tends to perform well regardless of the vertical grid being used. LES = large eddy simulations; BOMEX = Barbados Oceanographic Meteorological Experiment.

with the vertical resolution. The insensitivity of this parameterization to vertical resolution results from the explicit dependency of CF_{vol}, CF_{surf} or q_c to the layer thickness Δz .

4.3. Results From LMDzβ6 SCM Simulations

Until now in this paper, only LES have been used to develop and constrain the parameterizations, even if we may have degraded their vertical resolution to match the SCM vertical resolution.

In this section, we now implement the chosen Method 2 in the LMDzβ6 SCM and present its results on the 79 levels vertical grid (LMDzβ6*). Figure 11 shows the vertical profiles of the CF_{vol}, CF_{surf}, and q_c in LMDzβ6* SCM simulations obtained using this new Method 2. Results from LES data obtained with direct calculations and from the LMDzβ6 SCM without this parameterization are also shown for comparison. Note that the control LMDzβ6 parameterization (blue lines) was calibrated on an older LES version in the ARM and BOMEX cases only (see Jam et al., 2013). The clouds generated by LMDzβ6* and LMDzβ6 interact in the same way with their environment, via autoconversion into precipitation, for example, as CF_{surf} is for now just used as a diagnostic variable.

Regarding results from LMDzβ6 (blue lines), we notice on the ARM case a general underestimation of the CF by 5% to 10%, on the RICO case a 400-m negative shift in the position of the cloud top (1,800 m in the LES and 1,400 m in the SCM), and on the BOMEX case both a general underestimation of the CF by up to 4% and a 200-m positive shift in the position of the cloud base (500 m in the LES and 700 m in the SCM). It is working noting that this simulation does not include the parameterization yet, and the CF by volume and by surface

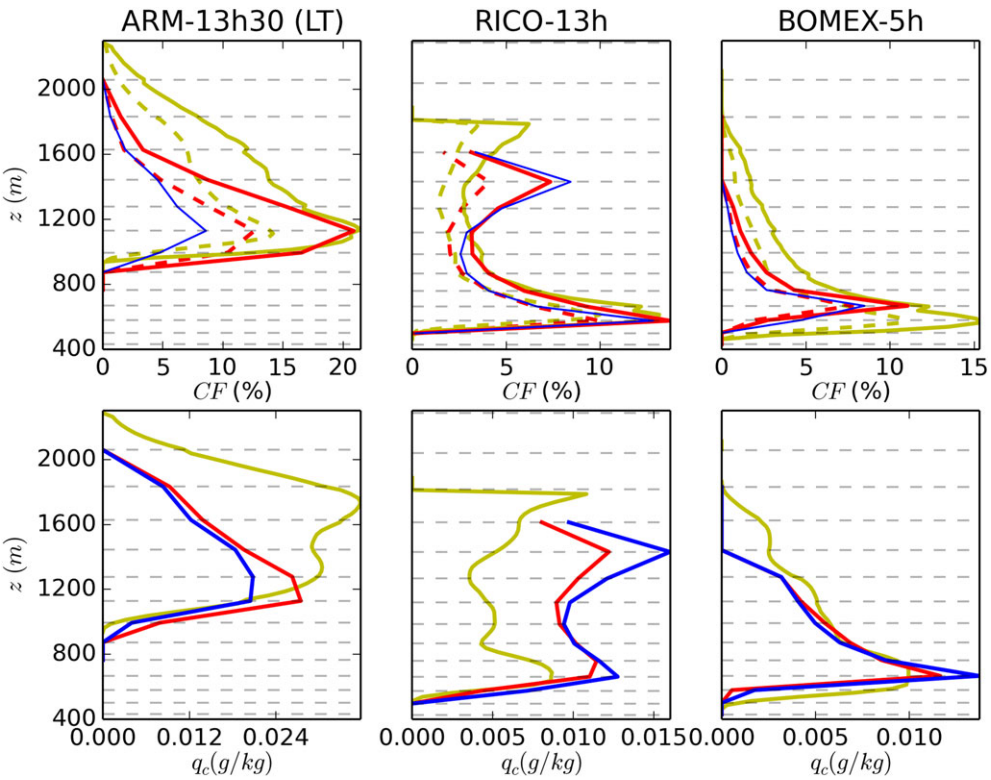

Figure 11. Vertical profiles of CF_{vol}, CF_{surf}, and q_c obtained using Method 2 in the LMDzβ6* SCM and compared to LES data and LMDzβ6. (top row) Dashed lines represent cloud fractions by volume CF_{vol} and solid lines cloud fractions by surface CF_{surf}. Yellow lines are the direct calculations using LES data gathered at the scale of the LMDzβ6 SCM grid boxes, red lines the results from the LMDzβ6* SCM based on Method 2, and blue lines the results from the LMDzβ6 SCM without the parameterization. We remind that no distinction is made between cloud fractions by volume and by surface in LMDzβ6. (bottom row) Condensed water q_c, same color code. LES = large eddy simulations; SCM = single column model; BOMEX = Barbados Oceanographic Meteorological Experiment.

are therefore equal by construction. We observe similar discrepancies on the condensed water q_c (bottom row) as can be expected by the strong dependency of q_c on CF.

Now switching to the LMDzβ6* results based on Method 2, we observe the same biased positions of the cloud base and top for the BOMEX and RICO cases, which we may be explained by the fact that the parameterization modifies the cloud structure at a subgrid scale only and only has minor effects on the macroscale. We also notice that CF_{surf} is well reproduced only when CF_{vol} is accurately estimated by the cloud scheme. Since CF_{surf} is a function of CF_{vol} in this parameterization, this behavior is expected. A general improvement appears in the ARM case up to 1,500 m and in the RICO case up to 1,100 m, where both CF_{vol} and CF_{surf} are simulated with an error of less than 1%. Method 2 explicitly distinguishes CF_{vol} from CF_{surf} and in general reduces the biases in q_c by about 20%.

Figure 12 shows the temporal evolution of the ARM CF by volume CF_{vol} and by surface CF_{surf} as simulated by the LMDzβ6* SCM and with LES data where layers are gathered at the scale of the SCM vertical ones. The LMDzβ6* SCM tends to overestimate the fractions both by volume and by surface between 11 and 13 hr, when the clouds start forming. After 13 hr, the fractions above 1,500 m are underestimated by up to 10%. We notice that this phenomenon that appears at 13h30, as shown in Figure 11, is present until the end of the simulation. It is also present in simulations performed using LMDzβ6 without Method 2 (not shown), which suggests that it comes from other aspects of the GCM.

4.3.1. Impacts on Radiation

In this section we analyze the radiative impacts of Method 2 on the LMDzβ6* SCM results. We remind that the heating rates are prescribed at each level independently from the parameterizations we test and that the radiative fluxes are computed for diagnostic purposes. A key variable for radiation is the cloud cover CF_{tot}. In LMDzβ6, it is computed using a maximum random overlap scheme, as mentioned in Geleyn and

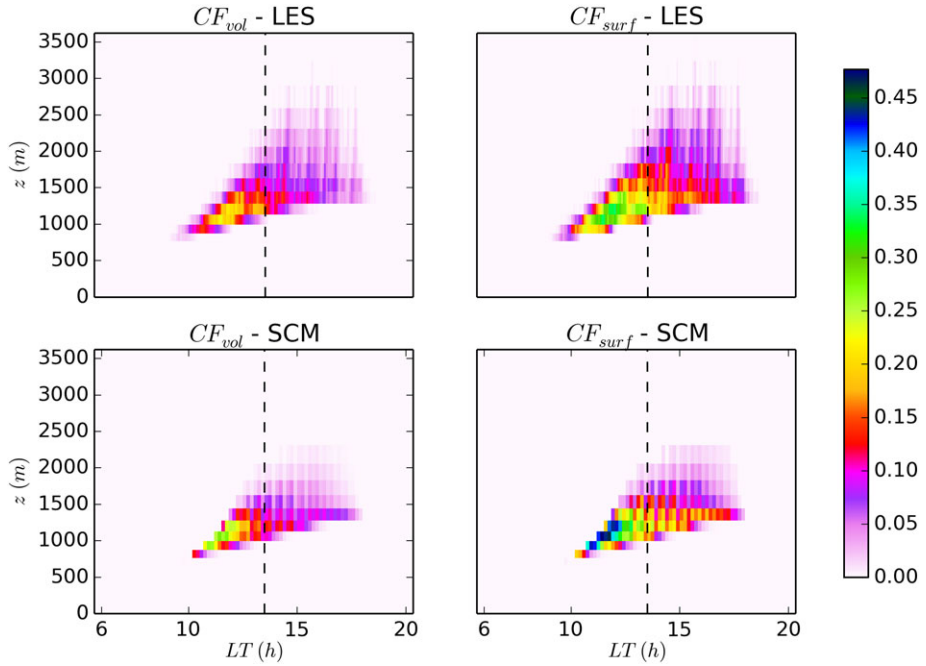

Figure 12. Temporal evolution of the cloud fractions by volume CF_{vol} (left column) and by surface CF_{surf} (right column) in the ARM case. Comparison between the LES (top row) and the LMDzβ6* SCM (bottom row). The black dashed vertical lines indicate the time when vertical profiles of cloud fractions and condensed water are shown in the rest of the paper. LES = large eddy simulations; SCM = single column model.

Hollingsworth (1979), Tian and Curry (1989), Barker et al. (1999), or Hogan and Illingworth (2000). Figure 13 shows the change in cloud cover at the surface CF_{tot}, the change in SW CRE (raw and normalized by the cloud cover), and the change in the liquid water path when the CF and condensed water are parameterized differently. Method 2 (in red) tends to increase the total cloud cover over the whole simulations by about 10% for RICO and BOMEX cases and by up to 50% for the ARM case when compared to the control simulation LMDzβ6 (blue lines). This is expected as the overlap scheme uses a CF_{surf} at each level which is mathematically greater or equal to the CF of the LMDzβ6 simulation. The liquid water path is globally reduced by 10–20% in the RICO and BOMEX cases. This is consistent with Figure 11 and due to a decrease in q_c of up to 20% when Method 2 is used.

The third row of Figure 13 shows a general decrease of the SW cloud radiative effect when normalized by CF_{tot}. Considering only cloud cover, these plots highlight the decrease of cloud opacities in the SW when using Method 2. This decrease in cloud cover is expected based on the general decrease in liquid water path which goes from less than 10% in the RICO case, to 25% in the ARM case and up to 70% in the BOMEX case. The bottom row of Figure 13 represents the raw SW CRE and shows that the larger cloud covers CF_{tot} are partly compensated by the decrease of cloud opacities. It still reduces the opacities of the atmospheric columns over the whole grid boxes for the three test cases. The mean decrease in SW CRE range from less than 5% in the ARM and RICO cases to 30–50% in the BOMEX case. Note that no SGS heterogeneity of condensed water q_c is taken into account in the radiative transfer scheme in this study. As mentioned by Cahalan et al. (1994), considering this effect could reduce even more the value of the SW CRE. Generally, these features obtained using Method 2 show a decrease of the too few, too bright bias by simulating larger low-level cloud covers and a generally lower opacity of the atmospheric column.

5. Conclusions

In this paper we aim at improving the representation of low-level clouds in the LMDzβ6 SCM with a focus on the continental and oceanic shallow cumulus cases ARM, RICO, and BOMEX. We develop and compare two parameterizations of the vertical SGS heterogeneity of cloud properties. We start from the cloud scheme presented in Jam et al. (2013) that is based on a horizontal SGS heterogeneity of saturation deficit s and propose two methods to also include vertical heterogeneity. Method 1 combines a vertical PDF of saturation deficit s to

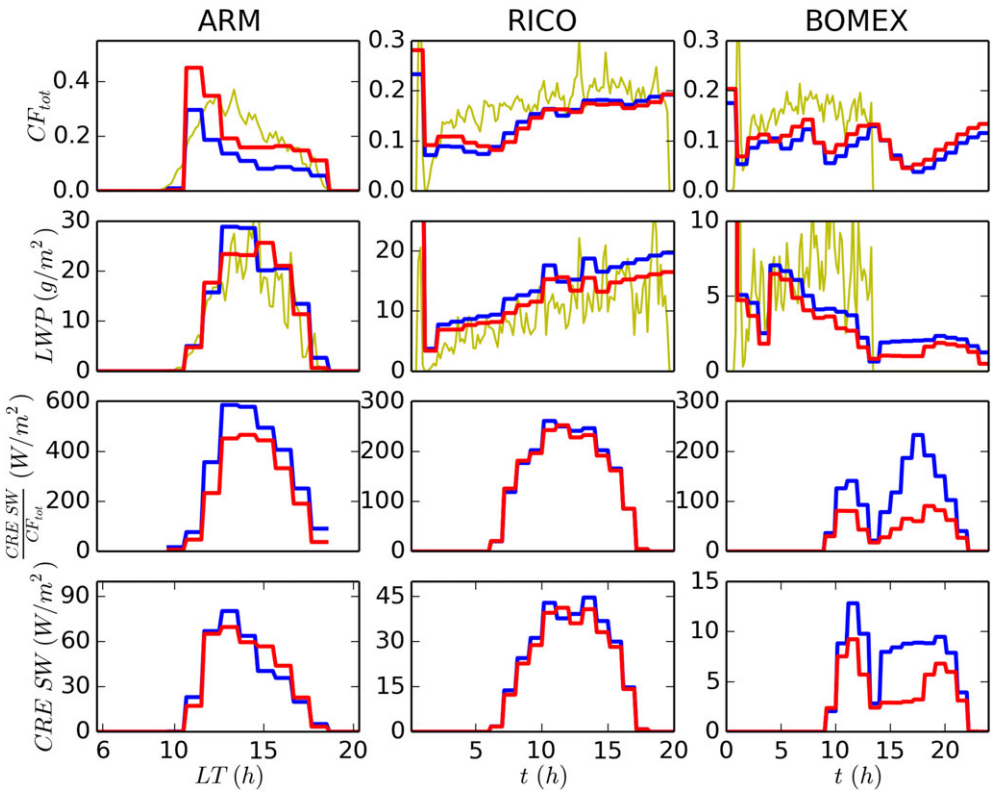

Figure 13. Temporal evolutions of the cloud cover CF_{tot} in the atmospheric column (first row), of the liquid water path *LWP* (second row), of the SW CRE normalized by the cloud cover $\frac{CRE\,SW}{CF_{tot}}$ (third row), and of the SW CRE (fourth row) for LMDzβ6* (red lines, with the Method 2), LMDzβ6 (blue lines, without the parameterization) and LES data (yellow lines). Note that for the stationary cases RICO and BOMEX, we impose an artificial diurnal cycle of the SW radiation in the SCM that impacts on the CRE diagnostics but not on the simulation itself. The Sun is up between 6 a.m. and 6 p.m. in the RICO case and between 9 a.m. and 10 p.m. in the BOMEX case. The BOMEX case is simulated over 24 hr, whereas the BOMEX LES lasts only 15 hr. Method 2 increases the cloud cover and reduces the liquid water path as well as the normalized SW CRE for all cases. It produces larger cloud fractions and less opaque clouds, resulting in a reduction of the *too few, too bright* bias. SW = shortwave; LES = large eddy simulations; BOMEX = Barbados Oceanographic Meteorological Experiment.

the horizontal existing one. The variances of the vertical PDF are parameterized as functions of the moments of the horizontal PDF and of the thickness of the layer Δz. The CF by volume CF_{vol} and the condensed water q_c are estimated by this combination of PDFs. The CF by surface CF_{surf} is estimated from the horizontal PDF only. Method 2 changes the horizontal PDF to a PDF based on three-dimensional statistics of saturation deficit *s*. It relies on the Jam et al. (2013) parameterization but introduces a dependency of the tunable parameters to the thickness of the layer. The quantities are calculated by volume as the condensed water q_c, and the CF_{vol} are directly estimated by this PDF. The CF by surface CF_{surf} is based on an adapted version of the Neggers et al. (2011) model and depends on CF_{vol} as well as on the thickness of the layers Δz.

Considering LES only, when using an altered vertical resolution to match that of LMDzβ6, Method 1 performs reasonably well and CF by volume and by surface are in good agreement with the LES when the SCM is specifically calibrated for a given cloud scene. However, it is hardly applicable to a GCM as it is very case sensitive and thus hardly tunable on a large variety of cloud scenes. Method 2 creates better CF and allows a solid distinction between CF_{vol} and CF_{surf} in the SCM for various cloud scenes.

When implemented in the LMDzβ6 SCM, simulations using Method 2 show a general improvement in the CF and a decrease in the bias of condensed water of about 20% when verified against the same data sets used to tune the parameterizations. When considering the whole atmospheric column, we observe a general increase of the cloud cover by 10–80% on the different cumulus cases. This parameterization also reduces the SW cloud radiative effect at the surface by 5–50% and does not impact significantly the LW radiation (decrease of 2–5%, not shown). These trends tend to validate the hypothesis made by Konsta et al. (2016) that stipulates

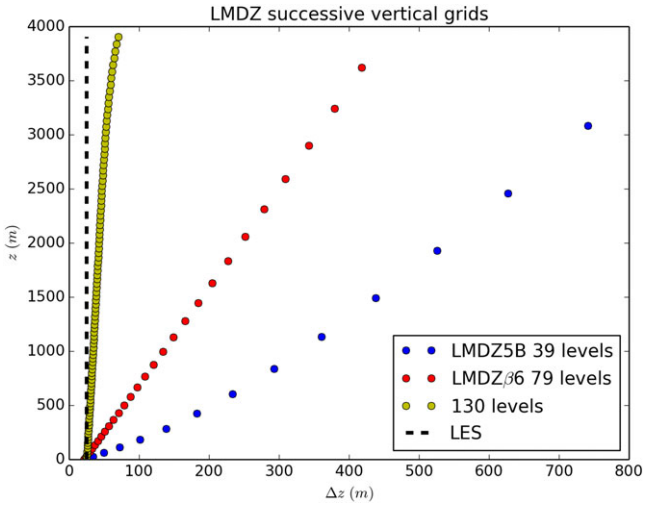

Figure 14. Layer height z as a function of layer depth Δz for successive versions of LMDz and for the LES, represented over the first 4,000 m of the atmosphere. LDMZ5B 39 levels grid: $\frac{\Delta z}{z} \sim 0.3$. LMDz$\beta$6 79 levels grid: $\frac{\Delta z}{z} \sim 0.1$. Testing 130 levels grid: $\frac{\Delta z}{z} \sim 0.01$. LES grid: $\Delta z = 25$ m, independent from altitude z. LES = large eddy simulations.

that taking into account vertical SGS heterogeneity in a GCM cloud scheme could reduce the too few, too bright bias by increasing the cloud cover and reducing the reflectance and opacity of such cloud scenes.

The next step is to implement Method 2 in the LMDz GCM, to tune the relevant parameters, and to analyze the results obtained at a global scale. At this stage, other well documented-parameterizations should also be coupled to Method 2 in order to assess their effects. First, in the radiation scheme of the LMDz GCM, the clouds are considered to be horizontally homogeneous. This leads to an overestimation of the emissivity and albedo by 2–18 W/m^2. Correcting this approximation that impacts the SW CRE by taking into account the heterogeneity of clouds would interact with Method 2, and this deserves further analysis. Second, the LMDz GCM uses a *maximum random* overlap scheme and does not include the more realistic *exponential random* overlap scheme from Hogan and Illingworth (2000). Such an overlap scheme would tend to again increase the cloud cover compared to what is done in this study. This global analysis is the subject of ongoing research by the authors.

Appendix A : Appendix

A1. Thermodynamic Constant a_l

Definition of the thermodynamic constant a_l from equation (1):

$$\begin{cases} T_l = T.e^{-\frac{q_l.L_v}{C_{pm}.T}} \\ q_{sl} = 0.622\frac{q_{sat}.L_v}{R_d.T_l^2} \\ a_l = \frac{1}{1+\frac{q_{sl}.L_v}{C_{pm}}} \end{cases} \tag{A1}$$

where q_l (kg/kg) is the liquid water content, $L_v(J/kg)$ the latent heat of vaporization, $C_{pm}(J/K)$ the heat capacity of moist air, q_{sat} (kg/kg) the saturation mixing ratio, and $R_d(J/K/kg)$ the perfect gas constant for dry air.

A2. Vertical Resolutions of Successive Versions of LMDz in the Lower Atmosphere

Figure 14 presents vertical resolutions used in successive versions of LMDz.

A3. Developments of Equation (7) With the Parameterizations From Equations (2), (8), and (9)

Some constants:

$$\begin{cases} S_{1_{\text{th,env}}} = -\frac{1}{\sqrt{2}}\left(\frac{\bar{s}_{\text{th,env}}+\sigma_{z_{\text{th,env}}}}{\sigma_{h_{\text{th,env}}}}\right) \\ S_{2_{\text{th,env}}} = -\frac{1}{\sqrt{2}}\left(\frac{\bar{s}_{\text{th,env}}-\sigma_{z_{\text{th,env}}}}{\sigma_{h_{\text{th,env}}}}\right) \end{cases} \tag{A2}$$

Development of the condensed water q_c:

$$q_c = \alpha q_{c_{\text{th}}} + (1-\alpha) q_{c_{\text{env}}} \tag{A3}$$

$$\begin{cases} q_{c_{\text{th,env}}} = q_{\Delta_{th1,env1}} + q_{\Delta_{th2,env2}} + q_{\Delta_{\text{th3,env3}}} + q_{\infty_{\text{th,env}}} \\ q_{\Delta_{\text{th1,env1}}} = \frac{\left(\bar{s}_{\text{th,env}} + \sigma_{z_{\text{th,env}}}\right)^2 + \sigma^2_{h_{\text{th,env}}}}{8\sigma_{z_{\text{th,env}}}} \left(erfS_{2_{\text{th,env}}} - erfS_{1_{\text{th,env}}} \right) \\ q_{\Delta_{\text{th2,env2}}} = \frac{\sigma^2_{h_{\text{th,env}}}}{4\sigma_{z_{\text{th,env}}}\sqrt{\pi}} \left(S_{1_{\text{th,env}}} e^{-S^2_{1_{\text{th,env}}}} - S_{2_{\text{th,env}}} e^{-S^2_{2_{\text{th,env}}}} \right) \\ q_{\Delta_{\text{th3,env3}}} = \sqrt{\frac{2}{\pi}} \frac{\sigma_{h_{\text{th,env}}} \left(\bar{s}_{\text{th,env}} + \Delta z\right)}{4\sigma_{z_{\text{th,env}}}} \left(e^{-S^2_{1_{\text{th,env}}}} - e^{-S^2_{2_{\text{th,env}}}} \right) \\ q_{\infty_{\text{th,env}}} = \frac{\bar{s}_{\text{th,env}}}{2} \left(1 - erf\left(S_{2_{\text{th,env}}} \right) \right) + \frac{\sigma_{h_{\text{th,env}}}}{\sqrt{2\pi}} . e^{-S^2_{2_{\text{th,env}}}} \end{cases} \tag{A4}$$

Development of the CF by volume CF_{vol}:

$$CF_{\text{vol}} = \alpha CF_{\text{vol}_{\text{th}}} + (1-\alpha) CF_{\text{vol}_{\text{env}}} \tag{A5}$$

$$\begin{cases} CF_{\text{vol}_{\text{th,env}}} = CF_{\Delta_{\text{th,env}}} + CF_{\infty_{\text{th,env}}} \\ CF_{\Delta_{\text{th,env}}} = \frac{\left(\bar{s}_{\text{th,env}} + \sigma_{z_{\text{th,env}}}\right)}{4\sigma_{z_{\text{th,env}}}} \left(\text{erfS}_{2_{\text{th,env}}} - \text{erfS}_{1_{\text{th,env}}} \right) + \sqrt{\frac{2}{\pi}} \frac{\sigma_{h_{\text{th,env}}}}{4\sigma_{z_{\text{th,env}}}} \left(e^{-S^2_{1_{\text{th,env}}}} - e^{-S^2_{2_{\text{th,env}}}} \right) \\ CF_{\infty_{\text{th,env}}} = \frac{1}{2} \left(1 - \text{erf}\left(S_{2_{\text{th,env}}} \right) \right) \end{cases} \tag{A6}$$

Development of the CF by surface CF_{surf}:

$$CF_{\text{surf}} = \alpha \left(\frac{1}{2} \left(1 - \text{erf}(S_{1_{\text{th}}}) \right) \right) + (1-\alpha) \left(\frac{1}{2} \left(1 - \text{erf}(S_{1_{\text{env}}}) \right) \right) \tag{A7}$$

Acronyms

GCM General circulation model
SCM Single column model
LES Large eddy simulation
SGS Subgrid scale
PDF Probability density function
CF Cloud fraction
SW Shortwave
LW Longwave

Acknowledgments
We acknowledge support from Agence Nationale de la Recherche (ANR) (grant HIGH-TUNE ANR-16-CE01-0010). This study benefited from the IPSL Prodiguer-Ciclad facility, which is supported by CNRS, UPMC, Labex L-IPSL, which is funded by the ANR (grant ANR-10-LABX-0018) and by the European FP7 IS-ENES2 project (grant 312979). We thank C. Rio, R. Roehrig, and M.P. Lefebvre for helpful discussions, comments, and suggestions. We thank the reviewers for the different comments they raised that helped improving the manuscript. No new data were used in producing this manuscript.

References

Barker, H. W., Stephens, G. L., & Fu, Q. (1999). The sensitivity of domain-averaged solar fluxes to assumptions about cloud geometry. *Quarterly Journal of the Royal Meteorological Society*, *125*(558), 2127–2152.
Barker, H. W., & Wielicki, B. A (1997). Parameterizing grid-averaged longwave fluxes for inhomogeneous marine boundary layer clouds. *Journal of the atmospheric sciences*, *54*(24), 2785–2798.
Bogenschutz, P. A., Gettelman, A., Morrison, H., Larson, V. E., Schanen, D. P., Meyer, N. R., & Craig, C. (2012). Unified parameterization of the planetary boundary layer and shallow convection with a higher-order turbulence closure in the Community Atmosphere Model: Single-column experiments. *Geoscientific Model Development*, *5*(6), 1407–1423.
Bogenschutz, P. A., Krueger, S. K., & Khairoutdinov, M. (2010). Assumed probability density functions for shallow and deep convection. *Journal of Advances in Modeling Earth Systems*, *2*, 24. https://doi.org/10.3894/JAMES.2010.2.10
Bony, S., & Dufresne, J.-L. (2005). Marine boundary layer clouds at the heart of tropical cloud feedback uncertainties in climate models. *Geophysical Research Letters*, *32*, L20806. https://doi.org/10.1029/2005GL023851
Bony, S., & Emanuel, K. A. (2001). A parameterization of the cloudiness associated with cumulus convection: Evaluation using TOGA COARE data. *Journal of the atmospheric sciences*, *58*(21), 3158–3183.
Bougeault, P. (1982). Cloud-ensemble relations based on the gamma probability distribution for the higher-order models of the planetary boundary layer. *Journal of the Atmospheric Sciences*, *39*(12), 2691–2700.
Boutle, I. A., Abel, S. J., Hill, P. G., & Morcrette, C. J. (2014). Spatial variability of liquid cloud and rain: Observations and microphysical effects. *Quarterly Journal of the Royal Meteorological Society*, *140*(679), 583–594.
Brooks, M. E., Hogan, R. J., & Illingworth, A. J. (2005). Parameterizing the difference in cloud fraction defined by area and by volume as observed with radar and lidar. *Journal of the atmospheric sciences*, *62*(7), 2248–2260.

Brown, A. R., Cederwall, R. T., Chlond, A., Duynkerke, P. G., Golaz, J.-C., Khairoutdinov, M., et al. (2002). Large-eddy simulation of the diurnal cycle of shallow cumulus convection over land. *Quarterly Journal of the Royal Meteorological Society*, *128*(582), 1075–1093.

Cahalan, R. F., Ridgway, W., Wiscombe, W. J., Bell, T. L., & Snider, J. B. (1994). The albedo of fractal stratocumulus clouds. *Journal of the Atmospheric Sciences*, *51*(16), 2434–2455.

Caniaux, G., Redelsperger, J. L., & Lafore, P. J. (1994). A numerical study of the stratiform region of a fast-moving squall line. Part I: General description and water and heat budgets. *Journal of the atmospheric sciences*, *51*(14), 2046–2074.

Cheng, A., & Xu, K.-M. (2015). Improved low-cloud simulation from the Community Atmosphere Model with an advanced third-order turbulence closure. *Journal of Climate*, *28*(14), 5737–5762.

Couvreux, F., Hourdin, F., & Rio, C. (2010). Resolved versus parametrized boundary-layer plumes. Part I: A parametrization-oriented conditional sampling in large-eddy simulations. *Boundary-layer meteorology*, *134*(3), 441–458.

Cuxart, J., Bougeault, P., & Redelsperger, J-L (2000). A turbulence scheme allowing for mesoscale and large-eddy simulations. *Quarterly Journal of the Royal Meteorological Society*, *126*(562), 1–30.

Del Genio, A. D., Yao, M.-S., Kovari, W., & Lo, K. K. (1996). A prognostic cloud water parameterization for global climate models. *Journal of Climate*, *9*(2), 270–304.

Geleyn, J. F., & Hollingsworth, A. (1979). An economical analytical method for the computation of the interaction between scattering and line absorption of radiation. *Contributions to Atmospheric Physics*, *52*, 1–16.

Golaz, J.-C., Larson, V. E., & Cotton, W. R. (2002). A PDF-based model for boundary layer clouds. Part I: Method and model description. *Journal of the atmospheric sciences*, *59*(24), 3540–3551.

Hogan, R. J., & Illingworth, A. J. (2000). Deriving cloud overlap statistics from radar. *Quarterly Journal of the Royal Meteorological Society*, *126*(569), 2903–2909.

Hourdin, F., Grandpeix, J.-Y., Rio, C., Bony, S., Jam, A, Cheruy, F., et al. (2013). LMDZ5B: the atmospheric component of the IPSL climate model with revisited parameterizations for clouds and convection. *Climate Dynamics*, *40*(9-10), 2193–2222.

Jam, A., Hourdin, F., Rio, C., & Couvreux, F. (2013). Resolved versus parametrized boundary-layer plumes. Part III: Derivation of a statistical scheme for cumulus clouds. *Boundary-layer meteorology*, *147*(3), 421–441.

Kawai, H., & Teixeira, J. (2012). Probability density functions of liquid water path and total water content of marine boundary layer clouds: Implications for cloud parameterization. *Journal of Climate*, *25*(6), 2162–2177.

Konsta, D., Dufresne, J.-L., Chepfer, H., Idelkadi, A., & Cesana, G. (2016). Use of a-train satellite observations (calipso—parasol) to evaluate tropical cloud properties in the lmdz5 gcm. *Climate Dynamics*, *47*(3-4), 1263–1284.

Lac, C., Chaboureau, P., Masson, V., Pinty, J.-P, Tulet, P., Escobar, J., et al. (2018). Overview of the Meso-NH model version 5.4 and its applications. *Geoscientific Model Development Discussions*, *11*, 1929–1969.

Larson, V. E., Golaz, J.-C., & Cotton, W. R. (2002). Small-scale and mesoscale variability in cloudy boundary layers: Joint probability density functions. *Journal of the atmospheric sciences*, *59*(24), 3519–3539.

Larson, V. E., & Schanen, D. P. (2013). The subgrid importance latin hypercube sampler (SILHS): A multivariate subcolumn generator. *Geoscientific Model Development*, *6*(5), 1813–1829.

Larson, V. E., Wood, R., Field, P. R., Golaz, J.-C., Haar, T. H. V., & Cotton, W. R. (2001). Small-scale and mesoscale variability of scalars in cloudy boundary layers: One-dimensional probability density functions. *Journal of the atmospheric sciences*, *58*(14), 1978–1994.

Le Treut, H., & Li, Z.-X. (1991). Sensitivity of an atmospheric general circulation model to prescribed SST changes: Feedback effects associated with the simulation of cloud optical properties. *Climate Dynamics*, *5*(3), 175–187.

LeMone, M. A., & Pennell, W. T (1976). The relationship of trade wind cumulus distribution to subcloud layer fluxes and structure. *Monthly Weather Review*, *104*(5), 524–539.

Lewellen, W. S., & Yoh, S. (1993). Binormal model of ensemble partial cloudiness. *Journal of the atmospheric sciences*, *50*(9), 1228–1237.

Li, J., Dobbie, S., Räisänen, P., & Min, Q. (2005). Accounting for unresolved clouds in a 1-D solar radiative-transfer model. *Quarterly Journal of the Royal Meteorological Society: A journal of the atmospheric sciences, applied meteorology and physical oceanography*, *131*(608), 1607–1629.

Mellor, G. L (1977). The Gaussian cloud model relations. *Journal of the Atmospheric Sciences*, *34*(2), 356–358.

Nam, C., Bony, S., Dufresne, J.-L., & Chepfer, H. (2012). The 'too few, too bright' tropical low-cloud problem in CMIP5 models. *Geophysical Research Letters*, *39*, L21801. https://doi.org/10.1029/2012GL053421

Neggers, R. A. J. (2009). A dual mass flux framework for boundary layer convection. Part II: Clouds. *Journal of the Atmospheric Sciences*, *66*(6), 1489–1506.

Neggers, R. A. J., Heus, T., & Siebesma, A. P. (2011). Overlap statistics of cumuliform boundary-layer cloud fields in large-eddy simulations. *Journal of Geophysical Research*, *116*, D21202. https://doi/org/10.1029/2011JD015650

Neggers, R. A. J., Siebesma, A. P., Lenderink, G., & Holtslag, A. A. M. (2004). An evaluation of mass flux closures for diurnal cycles of shallow cumulus. *Monthly weather review*, *132*(11), 2525–2538.

Perraud, E., Couvreux, F., Malardel, S., Lac, C., Masson, V., & Thouron, O. (2011). Evaluation of statistical distributions for the parametrization of subgrid boundary-layer clouds. *Boundary-layer meteorology*, *140*(2), 263–294.

Pincus, R., & Klein, S. A. (2000). Unresolved spatial variability and microphysical process rates in large-scale models. *Journal of Geophysical Research*, *105*(D22), 27059–27065.

Pinty, J.-P., & Jabouille, P. (1998). 6B. A mixed-phased cloud parameterization for use in a mesoscale non-hydrostatic model: Simulations of a squall line and of orographic precipitation. In *Conference on Cloud Physics: 14th Conference on Planned and Inadvertent Weather Modification* 17–21 August, Everett, WA. .

Rio, C., & Hourdin, F. (2008). A thermal plume model for the convective boundary layer: Representation of cumulus clouds. *Journal of the atmospheric sciences*, *65*(2), 407–425.

Rio, C., Hourdin, F., Couvreux, F., & Jam, A. (2010). Resolved versus parametrized boundary-layer plumes. Part II: Continuous formulations of mixing rates for mass-flux schemes. *Boundary-layer meteorology*, *135*(3), 469–483.

Siebesma, A. P., Bretherton, C. S., Brown, A., Chlond, A., Cuxart, J., Duynkerke, P. G., et al. (2003). A large eddy simulation intercomparison study of shallow cumulus convection. *Journal of the Atmospheric Sciences*, *60*(10), 1201–1219.

Sommeria, G., & Deardorff, J. W. (1977). Subgrid-scale condensation in models of nonprecipitating clouds. *Journal of the Atmospheric Sciences*, *34*(2), 344–355.

Tian, L., & Curry, J. A (1989). Cloud overlap statistics. *Journal of Geophysical Research*, *94*(D7), 9925–9935.

Tompkins, A. M. (2002). A prognostic parameterization for the subgrid-scale variability of water vapor and clouds in large-scale models and its use to diagnose cloud cover. *Journal of the atmospheric sciences*, *59*(12), 1917–1942.

VanZanten, M. C., Stevens, B., Nuijens, L., Siebesma, A. P., Ackerman, A. S., Burnet, F., et al. (2011). Controls on precipitation and cloudiness in simulations of trade-wind cumulus as observed during RICO. *Journal of Advances in Modeling Earth Systems*, *3*, M06001. https://doi.org/10.1029/2011MS000056

Vial, J., Dufresne, J.-L., & Bony, S. (2013). On the interpretation of inter-model spread in CMIP5 climate sensitivity estimates. *Climate Dynamics*, *41*(11-12), 3339–3362.

Zelinka, M. D., Randall, D. A., Webb, M. J., & Klein, S. A. (2017). Clearing clouds of uncertainty. *Nature Climate Change*, *7*(10), 674–678.

Zhang, Y., Klein, S. A., Fan, J., Chandra, A. S., Kollias, P., Xie, S., & Tang, S. (2017). Large-eddy simulation of shallow cumulus over land: A composite case based on ARM long-term observations at its Southern Great Plains site. *Journal of the Atmospheric Sciences*, *74*(10), 3229–3251.

Zhang, M. H., Lin, W. Y., Klein, S. A., Bacmeister, J. T., Bony, S., Cederwall, R. T., et al. (2005). Comparing clouds and their seasonal variations in 10 atmospheric general circulation models with satellite measurements. *Journal of Geophysical Research*, *110*(D15S02). https://doi.org/10.1029/2004JD005021